Journal of Materials Chemistry C

ROYAL SOCIETY OF CHEMISTRY

PAPER

View Article Online
View Journal | View Issue

Cite this: J. Mater. Chem. C, 2022, 10, 4614

Highly efficient blue electroluminescence based on TADF emitters with spiroacridine donors: methyl group effect on photophysical properties†

Han Xia,‡[a] Yukun Tang,‡[b] Youming Zhang,‡[a] Fan Ni,*[c] Yuntao Qiu,[a] Chih-Wei Huang,[b] Chung-Chih Wu*[b] and Chuluo Yang*[a]

Received 14th October 2021,
Accepted 24th November 2021

DOI: 10.1039/d1tc04939a

rsc.li/materials-c

The methyl group plays an important role in the regulation of the photoluminescence and electroluminescence properties of thermally activated delayed fluorescence (TADF) emitters. In this work, a new type of methyl effect was revealed by designing donor–accepter–donor (D–A–D) type TADF systems with decorating methyl groups at the *ortho*-position of the donor units. Different from previous work in which the methyl groups at the *ortho*-position resulted in improved TADF properties, the insertion of methyl groups in this work led to the reduction of the molecular rigidity, the photoluminescence quantum yield (PLQY) and the ratio of delayed fluorescence, as well as the extension of the lifetime of delayed fluorescence. The unusual changes of the photoluminescence behavior were well explained by theoretical simulations and further verified by the performance in electroluminescence devices. The blue organic light-emitting diodes (OLEDs) based on the new emitters achieved a maximum external quantum efficiency (EQE) of 19.3%.

1. Introduction

In the last decade, thermally activated delayed fluorescence (TADF) materials have been extensively studied as excellent emitters for organic light-emitting diodes (OLEDs) due to their outstanding photoelectric properties.[1] TADF materials can transform a triplet exciton into a singlet exciton through the efficient reverse intersystem crossing (RISC) process and then experience a radiative process to give out delayed fluorescence, thus enabling OLEDs with a theoretical 100% internal quantum efficiency (IQE).[2] The ideal TADF materials can be defined as those emitters that have a high photoluminescence quantum yield (PLQY), a short lifetime (τ_d) and a high ratio (r_d) of delayed fluorescence.[3] To obtain these properties, it is necessary to precisely design the molecular structure to regulate the behavior of the excited state as even small changes can obviously affect the photophysical and electroluminescence (EL) performance.

Serving as the smallest alkyl group, the methyl group demonstrates a weak hyperconjugation effect and a steric hindrance effect when linked to an aromatic ring.[4] The methyl group plays an important role in the design of TADF materials where three types of methyl effects can be concluded.[5–10] Type 1: the introduction of methyl groups can effectively improve the luminescence performance of TADF materials. The Adachi[5] and Monkman[6] groups have revealed that methyl decorated molecules displayed more ideal TADF properties. Type 2: the introduction of methyl groups can switch on the TADF feature in some systems, clearly indicating the small group but the remarkable effect. Ding[7] and Li[8] *et al.* have proved that methyl groups can be the key for the activation of the RISC channel. Type 3: methyl groups can even switch off the TADF behavior and turn on the room temperature phosphorescence (RTP). Bryce[9] and Kim[10] both have found that introducing methyl groups can be unfavorable for the RISC process such that the delayed fluorescence cannot be generated.

In type 1, the sole decoration of the methyl group at the *ortho*-position of the donor units in TADF materials usually meant the improvement of the molecular rigidity, PLQY and ratio of delayed fluorescence, and the shortening of the lifetime of delayed fluorescence. In this work, diphenyl sulfone (DPS) and 10*H*-spiro[acridine-9,8′-indolo[3,2,1-*de*]acridine] (SAIA) were used as the acceptor and donor units to design TADF molecules.

[a] *Guangdong Research Center for Interfacial Engineering of Functional Materials, College of Materials Science and Engineering, Shenzhen University, Shenzhen 518060, P. R. China. E-mail: clyang@szu.edu.cn*
[b] *Department of Electrical Engineering, Graduate Institute of Electronics Engineering and Graduate Institute of Photonics and Optoelectronics, National Taiwan University, Taipei, 10617, Taiwan. E-mail: wucc@ntu.edu.tw*
[c] *School of Instrument Science and Optoelectronics Engineering, Department of Biomedical Engineering, Hefei University of Technology, Hefei 230009, P. R. China. E-mail: nfope@hfut.edu.cn*

† Electronic supplementary information (ESI) available. See DOI: 10.1039/d1tc04939a

‡ These authors contributed equally to this publication.

The two methyl groups were linked on two phenyls at the *ortho* position of the donor SAIA to obtain multiple beneficial effects to achieve more efficient blue-shifted emission. To our surprise, different results were found in this work. The measured photophysical properties of the two emitters (DPS–SAIA and Me–DPS–SAIA) revealed that the emission band of Me–DPS–SAIA with decorated methyl groups did demonstrate an obvious blue shift. However, the molecular rigidity, the rate constant of the RISC process, and the PLQY were all reduced, which are not quite the same as the previous results of the type 1 methyl effect. The theoretical simulation proved the enlarged energy gap (ΔE_{ST}) between the excited singlet–triplet (S_1–T_1) state, and the more flexible configuration in Me–DPS–SAIA, which are consistent with the photophysical properties of the prolonged lifetime of delayed fluorescence and a decreased PLQY. Moreover, the electroluminescence performance of the two emitters further confirmed the unexpected methyl effect.

2. Results and discussion

2.1 Molecular design and synthesis

In this work, a fixed and three-dimensional unit of 10*H*-spiro-[acridine-9,8′-indolo[3,2,1-*de*]acridine] (SAIA) with the integration of acridine and phenyl-carbazole was used as the electron donor and diphenylsulfone (DPS) was used as the electron acceptor. The direct combination of the two SAIA donors and one DPS acceptor constructed the D–A–D type molecule of DPS–SAIA. To investigate the methyl effect, two methyl groups were settled at the *ortho* position of the two SAIA donors and the control molecule of Me–DPS–SAIA was designed. The two methyl substituents were decorated to fine tune the weak electron-donating ability of the acceptor and the photophysical properties of the two designed emitters.

The synthetic routes for the donor SAIA and the target compounds of DPS–SAIA and Me–DPS–SAIA are shown in Scheme 1 and Scheme S1 (ESI†). The donor SAIA was synthesized through the classical pathway for the construction of the spiroacridine unit. DPS–SAIA and Me–DPS–SAIA were synthesized *via* a one-step Pd-catalyzed Buchwald–Hartwig C–N cross-coupling reaction. SAIA, DPS–SAIA, and Me–DPS–SAIA were characterized by ^{1}H NMR spectroscopy, and high-resolution mass spectrometry (HRMS) (see ESI,† Fig. S1–S7).

2.2 DFT calculations

Calculations based on density functional theory (DFT) and time-dependent DFT were conducted to simulate the ground (S_0) and excited molecular structures and properties.[11] The ground state molecular structures were optimized at the B3LYP/6-31G(d,p) level of theory. The energy gaps between the S_1 and T_1 states were calculated using the PBE0/def2-SVP theory. The configuration of the S_1 state was calculated at the B3LYP/def2-SVP level.

The molecular configurations and orbital distributions of the two molecules are shown in Fig. 1. It can be seen that both the two molecules exhibited distorted arrangements between the donor and acceptor units in the ground state. The dihedral angles between the diphenylsulfone and acridine units were both close to 90° for DPS–SAIA and Me–DPS–SAIA (Fig. S8, ESI†). The twisted D–A link mode facilitated the efficient separation between the HOMOs and LUMOs, with the HOMOs mainly located on the acridine unit and the LUMOs mainly centered on the diphenylsulfone unit. The limited overlap (on the acridine unit) between the HOMO and LUMO in the two molecules implied the small ΔE_{ST} values and the possible activated reverse intersystem crossing.

For the ground and excited energy levels, the simulated HOMO energy levels are identical (−5.25 eV) for the two molecules, which can be ascribed to the same donor unit and the similar HOMO distribution. Due to the weak electron-donating ability of methyl groups, the electron-withdrawing ability of diphenylsulfone in Me–DPS–SAIA is slightly weakened so that the LUMO energy level (−1.72 eV) of Me–DPS–SAIA is shallower than that (−1.84 eV) of DPS–SAIA. The natural transition orbital analysis demonstrated the charge transfer feature of the S_1 states of DPS–SAIA and Me–DPS–SAIA (Fig. 2). It can be expected that the relatively weaker electron-withdrawing ability of Me–DPS may lead to the weaker charge transfer strength, matching well with the simulated results of a relatively lower S_1 state energy level of 2.97 eV for DPS–SAIA but a higher energy level of 3.09 eV for Me–DPS–SAIA. The simulated T_1 state energy levels of DPS–SAIA and Me–DPS–SAIA were 2.95 and 2.97 eV, respectively. As a result, the twisted D–A–D arrangements in the two molecules enabled small ΔE_{ST}s of 0.02 eV for DPS–SAIA and 0.12 eV for Me–DPS–SAIA, which could efficiently facilitate the RISC process.

Then the comparison between the optimized ground state and excited state configurations of the two molecules was conducted (Fig. S8, ESI†). The geometries of the S_1 and S_0

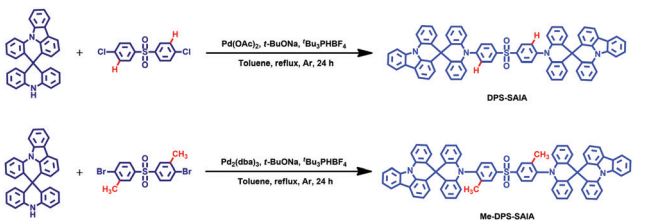

Scheme 1 Synthetic routes for DPS–SAIA and Me–DPS–SAIA.

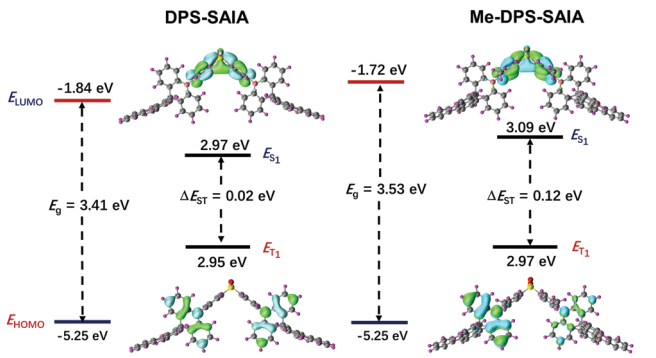

Fig. 1 The optimized molecular conformations, frontier molecular orbital distributions and energy levels of DPS–SAIA and Me–DPS–SAIA.

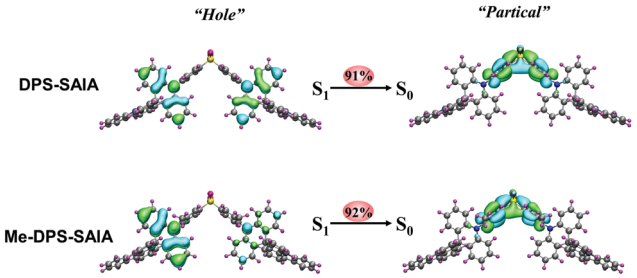

Fig. 2 The natural transition orbitals of DPS–SAIA and Me–DPS–SAIA.

states showed the deformation of the two emitters (Fig. S9, ESI†), and the root-mean-square-deviation (RMSD)[12] values of DPS–SAIA and Me–DPS–SAIA were 0.37 and 0.47 Å, respectively, indicating that the insertion of methyl groups introduced more flexibility in Me–DPS–SAIA. This result is contrary to our expectations. The further analysis revealed that the RMSD values between the donor SAIA at S_0 and S_1 states derived from DPS–SAIA and Me–DPS–SAIA were 0.08 Å and 0.11 Å, respectively, while the values between the acceptor DPS and Me–DPS at S_0 and S_1 states were 0.08 Å and 0.13 Å, respectively. The analysis of the dihedral angles between the sulfonyl group and the adjacent phenyl groups in the optimized ground state and excited state configurations revealed the enhanced structure rotation of the diphenylsulfone unit in Me–DPS–SAIA compared to that in DPS–SAIA (Fig. S10, ESI†). The inserted methyl groups with weak electron-donating ability affected the optimized configurations of the acceptor unit and further caused the increased flexibility of the whole molecule. The above results indicated that the inserted methyl groups resulted in more configuration changes of the donor and acceptor units after excitation.

2.3 Thermal and electrochemical properties

Thermogravimetric analysis (TGA) and differential scanning calorimeter (DSC) measurements were then conducted to evaluate the thermal properties of the two materials. As shown in Fig. 3, DPS–SAIA and Me–DPS–SAIA both revealed good thermal stability with the decomposition temperatures (T_d, defined as 5% weight loss) over 500 °C. No T_g was detected during the DSC experiments for the two compounds, demonstrating their high morphological stability.

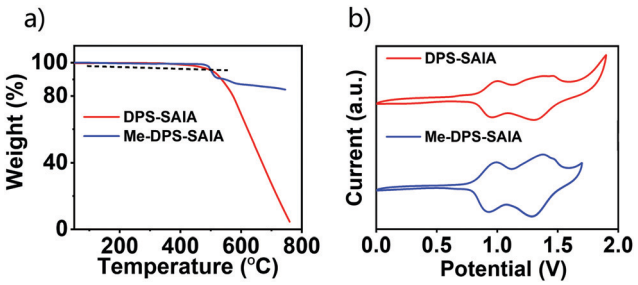

Fig. 3 (a) TGA curves and (b) cyclic voltammetry curves of DPS–SAIA and Me–DPS–SAIA.

The cyclic voltammetry curves of the two compounds in dichloromethane solutions were measured to evaluate the frontier molecular orbital energy levels. Determined by the onset of the oxidation curves, the HOMO energy levels of DPS–SAIA and Me–DPS–SAIA were −5.17 eV and −5.16 eV, respectively, well matching with the same donor unit in the two molecules. The LUMO energy levels obtained from E_{HOMO} and E_g were −2.20 eV for DPS–SAIA and −2.14 eV for Me–DPS–SAIA, consistent with the trend of the theoretical simulation.

2.4 Photophysical properties

To further confirm the TADF feature of the two emitters, photophysical properties were then investigated. As shown in Fig. 4a and b, the strong absorption band with a wavelength shorter than 370 nm can be ascribed to the localized state transitions, and the relatively broad absorption band from 370 to 400 nm can be attributed to the intramolecular charge transfer (ICT) transitions of the two compounds. The fluorescence spectra of the two molecules in toluene solutions revealed the broad structureless emission, demonstrating the typical charge transfer feature of the S_1 states. With the decoration of two methyl groups in Me–DPS–SAIA, a weakened charge transfer S_1 state was found and the emission peak (442 nm) in toluene solution revealed a slight blue shift compared to that (447 nm) of DPS–SAIA. The phosphorescence spectra measured at 77 K of the two compounds showed fine emission bands, indicating that the T_1 state originated from the locally excited (LE) transition. Compared to the measured phosphorescence spectra of the donor and acceptor units at 77 K, it can be concluded that the LE featured phosphorescence of the two molecules was derived from the donor unit (SAIA) (Fig. S11, ESI†). Determined from the onset of the fluorescence and phosphorescence spectra, the E_{S1}/E_{T1} values were calculated to be 3.04/3.01 eV for DPS–SAIA and 3.09/3.02 eV for Me–DPS–SAIA.

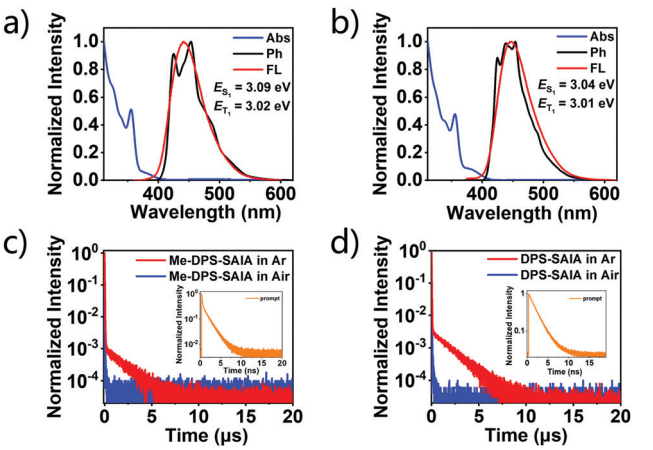

Fig. 4 (a) UV-vis absorption, fluorescence (room temperature) and phosphorescence (77 K) spectra of 10^{-5} M Me–DPS–SAIA in toluene solution. (b) UV-vis, fluorescence (room temperature) and phosphorescence (77 K) spectra of 10^{-5} DPS–SAIA in toluene solution. The transient photoluminescence decay curves of Me–DPS–SAIA (c) and DPS–SAIA (d) in toluene solutions.

Sufficiently small ΔE_{ST} values (0.03 eV for DPS–SAIA and 0.07 eV for Me–DPS–SAIA) were obtained in the two emitters, indicating that the RISC channel can be activated.

To confirm the TADF mechanism, the steady and transient photoluminescence spectra of DPS–SAIA and Me–DPS–SAIA in aerated and degassed toluene were then measured. The steady emissions of the two emitters in toluene solutions were both enhanced after degassing (Fig. S12, ESI†). According to transient decay measurements, both the emitters exhibited microsecond-scale emission and nanosecond-scale emission in deoxygenated toluene (Fig. 4c and d). The long-lived components of the two emitters were totally quenched after being exposed to air, clearly revealing that the microsecond-scale emission was derived from the excited triplet states. Taking a comparison of the transient photoluminescence decay of the two emitters in toluene, we can find that the delay ratio (31%) of DPS–SAIA without decorating methyl groups was higher than that (20%) of Me–DPS–SAIA. The smaller ΔE_{ST} value enabled DPS–SAIA to exhibit a shorter long-lifetime but a higher ratio of delayed fluorescence to that of Me–DPS–SAIA, implying the more efficient RISC channel without decorating methyl groups.

To simulate the emissive behavior in OLEDs, the basic photophysical properties of DPS–SAIA and Me–DPS–SAIA in bis[2-(diphenylphosphino)phenyl]-ether oxide (DPEPO) doped films were measured. As shown in Fig. 5a, the 12 wt% DPS–SAIA and Me–DPS–SAIA doped films emitted structureless blue light with the emission peaks centered at 460 and 449 nm, respectively. The broad emission bands with full widths at half maxima of 75 nm for DPS–SAIA and 78 nm for Me–DPS–SAIA revealed the typical charge transfer S_1 states of the two emitters. The transient photoluminescence spectra of the two doped films were also measured (Fig. 5b and c), both demonstrating nanosecond-scale and microsecond-scale transitions. The double fluorescence components clearly identified the TADF mechanism. The delayed fluorescence ratio (33%) of DPS–SAIA was higher than that (13%) of Me–DPS–SAIA, further revealing the more efficient RISC channel of DPS–SAIA in the doped films. To visually prove the luminescence mechanism, the steady and transient photoluminescence spectra of the two doped films at different temperatures were measured (Fig. S14, ESI†). The temperature-sensitive long-lived emission strongly confirmed the thermally activated delayed fluorescence mechanism in the two emitters.

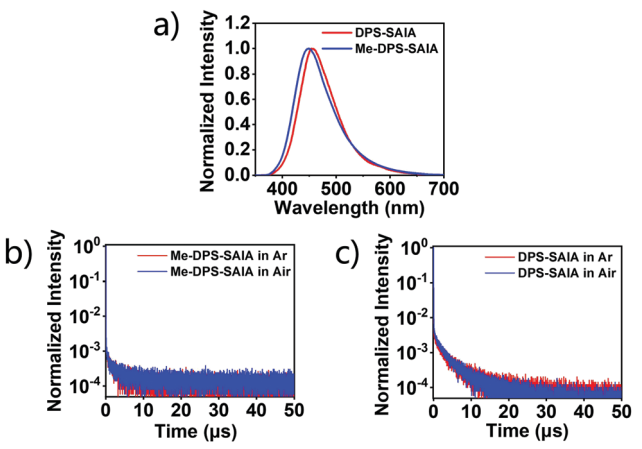

Fig. 5 (a) The fluorescence spectra of 12 wt% DPEPO doped films at room temperature. The transient photoluminescence decay curves of (b) 12 wt% Me–DPS–SAIA and (c) 12 wt% DPS–SAIA in DPEPO doped films at room temperature.

The PLQYs of DPS–SAIA and Me–DPS–SAIA doped DPEPO films were 66% and 60%, respectively. The relatively lower PLQY value of Me–DPS–SAIA doped DPEPO films matched well with the simulation results of the methyl-induced flexibility. To better evaluate the delayed fluorescence behavior, the rate constants of intersystem crossing (ISC), reverse intersystem crossing, singlet radiative and non-radiative transitions were calculated based on the basic photophysical data measured at room temperature. The larger ΔE_{ST} value resulted in the slower RISC process (1.1×10^5 s^{-1}) in Me–DPS–SAIA to that (2.3×10^5 s^{-1}) in DPS–SAIA. In addition, the radiation transition rate constants of the S_1 state ($k_{r,S}$) were 2.1×10^7 s^{-1} for DPS–SAIA and 1.0×10^7 s^{-1} for Me–DPS–SAIA. All the photophysical property data are listed in Tables 1 and 2.

2.5 Device performances

The obvious TADF properties of DPS–SAIA and Me–DPS–SAIA enabled them to be suitable emitters for fabricating blue OLEDs. The optimized OLEDs based on the two emitters were fabricated with the device configuration of ITO (80 nm)/MoO_3 (1 nm)/TAPC (45 nm)/mCP (10 nm)/DPEPO: emitter (12 wt%) (20 nm)/3TPYMB (50 nm)/LiF/Al (Fig. 6a, Fig. S16, ESI†). ITO and Al were used as the anode and the cathode, respectively; molybdenum trioxide (MoO_3) and LiF served as the hole and electron injection layers, respectively; 1,1-bis[(di-4-tolylamino)-phenyl]cyclohexane (TAPC) was used as the hole transport layer; tris(2,4,6-trimethyl-3-(pyridin-3-yl)phenyl)borane (3TPYM) acted as the electron transport and hole blocking layers; 1,3-di(9*H*-carbazol-9-yl)benzene (mCP) served as the electron barrier layer. Moreover, 12 wt% DPS–SAIA or Me–DPS–SAIA doped into the DPEPO host was the emitting layer (EML) in the device.

The introduction of methyl substitutions in Me–DPS–SAIA resulted in the blue-shifted photoluminescence and the same trend was found in the electroluminescence spectra (Fig. 6b, Table 3). The maximum emission peaks of DPS–SAIA and Me–DPS–SAIA were 474 and 458 nm, respectively. The sole blue emission indicated the efficient energy transfer from the DPEPO host to the TADF guests. The DPS–SAIA-doped device revealed a relatively higher maximum EQE (19.3%) than that of the Me–DPS–SAIA-based device (17.1%). To explain the relatively high EQEs to the moderate PLQYs, the angle dependent *p*-polarized photoluminescence intensity measurements were then measured for DPS–SAIA and Me–DPS–SAIA in the DPEPO host (12 wt%). The experimental $\Theta//s$ were both estimated to be 85% for the two doped films (Fig. S17, ESI†), which are much higher than that of the 67% of isotropic emitters. It is clear that the demonstrated high $\Theta//s$ could enable the effective optical out-coupling efficiency to guarantee the high electroluminescence performance. The EQEs of the two emitter-based devices

Table 1 Photophysical data of DPS–SAIA and Me–DPA–SAIA in toluene solutions

Compound	λ_{abs}[a] (nm)	λ_{PL}[a] (nm)	E_{HOMO}[b] (eV)	E_{LUMO}[b] (eV)	E_g[b] (eV)	E_{S1}[c] (eV)	E_{T1}[c] (eV)	ΔE_{ST}[c] (eV)
DPS–SAIA	355, 378	447	−5.17	−2.20	2.97	3.04	3.01	0.03
Me–DPS–SAIA	356, 375	442	−5.16	−2.14	3.02	3.09	3.02	0.07

[a] Measured in toluene solutions (10^{-5} M) at 298 K. [b] The E_{HOMO} values were calculated from cyclic voltammetry curves, and the E_g values (the optical energy gap) were obtained from the onset of the absorption spectra, $E_{LUMO} = E_{HOMO} + E_g$. [c] Estimated from the onset of the fluorescence (room temperature) and phosphorescence spectra (77 K) in toluene solutions (10^{-5} M).

Table 2 Photophysical data of 12 wt% DPS–SAIA and Me–DPA–SAIA in DPEPO doped films

Compound	Φ_{PL}[a] (%)	Φ_p[b] (%)	Φ_d[b] (%)	τ_p[c] (ns)	τ_d[c] (μs)	k_p[d] (10^7 s^{-1})	k_d[d] (10^4 s^{-1})	k_{ISC}[d] (10^7 s^{-1})	k_{RISC}[d] (10^5 s^{-1})	$k_{r,S}$[e] (10^7 s^{-1})	$k_{nr,S}$[e] (10^6 s^{-1})
DPS–SAIA	66	44	22	20.8	6.6	4.8	15.2	1.6	2.3	2.1	11.0
Me–DPS–SAIA	60	52	8	50.8	10.5	2.0	9.5	2.6	1.1	1.0	6.9

[a] Total PLQY (Φ_{PL}) of 12 wt% emitter-doped DPEPO film. [b] PLQYs of the prompt (Φ_p) and delayed (Φ_d) components. [c] Lifetimes of the prompt (τ_p) and delayed (τ_d) fluorescence. [d] The rate constants of ISC (k_{ISC}) and RISC (k_{RISC}) processes. [e] The rate constants of singlet radiative ($k_{r,S}$) and non-radiative ($k_{nr,S}$) transitions.

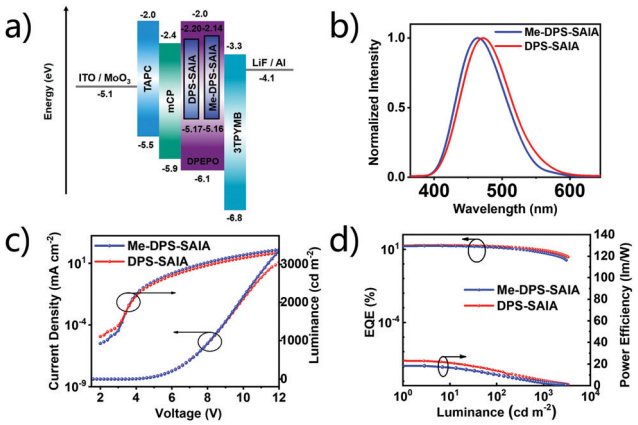

Fig. 6 (a) Device configuration and the energy level diagrams. (b) The EL spectra of DPS–SAIA and Me–DPS–SAIA-based devices. (c) Current density–voltage–luminescence (*J*–*V*–*L*) characteristics of the fabricated devices. (d) EQE–PE–L curves of the fabricated devices.

Table 3 Summary of the EL properties of 12 wt% doped devices

Emitter	EQE_{max}[a] (%)	EL_{Peak} (nm)	PE_{max}[b] (Im W^{-1})	CE_{max}[c] (cd A^{-1})	CIE[d] (*X*, *Y*)
Me–DPS–SAIA	17.1	464	13.8	27.0	(0.14, 0.16)
DPS–SAIA	19.3	472	18.1	30.4	(0.15, 0.20)

[a] Maximum external quantum efficiency. [b] Maximum power efficiency. [c] Maximum current efficiency. [d] CIE coordinates.

can remain 16.2% for DPS–SAIA and 13.1% for Me–DPS–SAIA at 100 cd m^{-2}. At 1000 cd m^{-2}, the EQEs of DPS–SAIA and Me–DPS–SAIA were 8.6% and 5.7%, respectively. The EQE roll-off at 100 and 1000 cd m^{-2} were 16% and 55% for the DPS–SAIA-based device but 23% and 67% for the Me–DPS–SAIA-based device. It is obvious that DPS–SAIA with a higher ratio but a shorter lifetime of delayed fluorescence resulted in the relatively slower EQE roll-off. The EQE values over 5% further confirmed the TADF feature of the two emitters and well demonstrated the effective utilization of triplet excitons during the electroluminescence process. The maximum current efficiency (CE) and power efficiency (PE) values of the two devices were 30.4 cd A^{-1} and 18.1 Im W^{-1} for the DPS–SAIA-based device and 27.0 cd A^{-1} and 13.8 Im W^{-1} for the Me–DPS–SAIA-based device.

3. Conclusions

In conclusion, the effect of decorating methyl groups in D–A–D type TADF systems was investigated by using the donor SAIA and the acceptor DPS. Similar to previous TADF systems with the sole decoration of the methyl group at the *ortho*-position of the donor units, the introduced methyl group in this work weakened the electron-withdrawing ability of the acceptor of DPS and led to blue-shifted emission. Interestingly, the inserted methyl groups caused different effects, including the increased ΔE_{ST} value, reduced molecular rigidity, and decreased PLQY. By analyzing the properties of the ground and excited states of the two emitters, theoretical simulations well explained the methyl effects. Finally, the devices based on the two emitters showed high performance with maximum EQEs of 19.3% and 17.1%, respectively.

Conflicts of interest

There are no conflicts to declare.

Acknowledgements

F. Ni gratefully acknowledges financial support from the National Natural Science Foundation of China (No. 51903161). C. Yang acknowledges the Shenzhen Science and Technology Program (KQTD20170330110107046), and the Instrumental Analysis Center of Shenzhen University for analytical support. C.-C. Wu acknowledges support from the Ministry of Science and Technology of Taiwan (MOST 107-2221-E-002-160-MY3 and 108-2221-E-002-148-MY3).

Notes and references

1 (*a*) Y. Tao, K. Yuan, T. Chen, P. Xu, H. Li, R. Chen, C. Zheng, L. Zhang and W. Huang, *Adv. Mater.*, 2014, **26**, 7931–7958; (*b*) S. O. Jeon, K. H. Lee, J. S. Kim, S.-G. Ihn, Y. S. Chung, J. W. Kim, H. Lee, S. Kim, H. Choi and J. Y. Lee, *Nat. Photonics*, 2021, **15**, 208–215; (*c*) C.-Y. Chan, M. Tanaka, Y.-T. Lee, Y.-W. Wong, H. Nakanotani, T. Hatakeyama and C. Adachi, *Nat. Photonics*, 2021, **15**, 203–207; (*d*) Z. Yang, Z. Mao, Z. Xie, Y. Zhang, S. Liu, J. Zhao, J. Xu, Z. Chi and M. P. Aldred, *Chem. Soc. Rev.*, 2017, **46**, 915–1016; (*e*) X. Cai and S.-J. Su, *Adv. Funct. Mater.*, 2018, **28**, 1802558; (*f*) M. Y. Wong and E. Zysman-Colman, *Adv. Mater.*, 2017, **29**, 1605444; (*g*) Y. Zou, S. Gong, G. Xie and C. Yang, *Adv. Opt. Mater.*, 2018, **6**, 1800568; (*h*) F. Ni, N. Li, L. Zhan and C. Yang, *Adv. Opt. Mater.*, 2020, **8**, 1902187; (*i*) D. Wang, C. Cheng, T. Tsuboi and Q. Zhang, *CCS Chem.*, 2020, **2**, 1278–1296; (*j*) T. T. Bui, F. Goubard, M. Ibrahim-Ouali, D. Gigmes and F. Dumur, *Beilstein J. Org. Chem.*, 2018, **14**, 282–308.

2 (*a*) H. Uoyama, K. Goushi, K. Shizu, H. Nomura and C. Adachi, *Nature*, 2012, **492**, 234–238; (*b*) Q. Zhang, B. Li, S. Huang, H. Nomura, H. Tanaka and C. Adachi, *Nat. Photonics*, 2014, **8**, 326–332; (*c*) Y. Im, M. Kim, Y. J. Cho, J.-A. Seo, K. S. Yook and J. Y. Lee, *Chem. Mater.*, 2017, **29**, 1946–1963; (*d*) W. Li, X. Cai, B. Li, L. Gan, Y. He, K. Liu, D. Chen, Y. C. Wu and S. J. Su, *Angew. Chem., Int. Ed.*, 2019, **58**, 582–586; (*e*) W. Zeng, T. Zhou, W. Ning, C. Zhong, J. He, S. Gong, G. Xie and C. Yang, *Adv. Mater.*, 2019, **31**, 1901404; (*f*) F. Ni, C.-W. Huang, Y. Tang, Z. Chen, Y. Wu, S. Xia, X. Cao, J.-H. Hsu, W.-K. Lee, K. Zheng, Z. Huang, C.-C. Wu and C. Yang, *Mater. Horiz.*, 2021, **8**, 547–555; (*g*) X. Zheng, R. Huang, C. Zhong, G. Xie, W. Ning, M. Huang, F. Ni, F. B. Dias and C. Yang, *Adv. Sci.*, 2020, **7**, 1902087.

3 (*a*) T. J. Penfold, F. B. Dias and A. P. Monkman, *Chem. Commun.*, 2018, **54**, 3926–3935; (*b*) Y. Chen, D. Zhang, Y. Zhang, X. Zeng, T. Huang, Z. Liu, G. Li and L. Duan, *Adv. Mater.*, 2021, **33**, 2103293; (*c*) X. Zeng, Y.-H. Huang, S. Gong, P. Li, W.-K. Lee, X. Xiao, Y. Zhang, C. Zhong, C.-C. Wu and C. Yang, *Mater. Horiz.*, 2021, **8**, 2286–2292; (*d*) J. U. Kim, I. S. Park, C. Y. Chan, M. Tanaka, Y. Tsuchiya, H. Nakanotani and C. Adachi, *Nat. Commun.*, 2020, **11**, 1765; (*e*) G. Xie, J. Luo, M. Huang, T. Chen, K. Wu, S. Gong and C. Yang, *Adv. Mater.*, 2017, **29**, 1604223.

4 (*a*) S. J. Woo, Y. Kim, S. K. Kwon, Y. H. Kim and J. J. Kim, *ACS Appl. Mater. Interfaces*, 2019, **11**, 7199–7207; (*b*) T. Serevicius, R. Skaisgiris, J. Dodonova, L. Jagintavicius, D. Banevicius, K. Kazlauskas, S. Tumkevicius and S. Jursenas, *ACS Appl. Mater. Interfaces*, 2020, **12**, 10727–10736; (*c*) J. Rao, L. Yang, X. Li, L. Zhao, S. Wang, H. Tian, J. Ding and L. Wang, *Angew. Chem., Int. Ed.*, 2021, **60**, 9635–9641; (*d*) D. Chai, Y. Zou, Y. Xiang, X. Zeng, Z. Chen, S. Gong and C. Yang, *Chem. Commun.*, 2019, **55**, 15125–15128; (*e*) Q. Lu, M. Qin, S. Liu, L. Lin, C.-K. Wang, J. Fan and Y. Song, *Chem. Phys. Lett.*, 2021, **764**, 138260; (*f*) I. E. Serdiuk, C. H. Ryoo, K. Kozakiewicz, M. Mońka, B. Liberek and S. Y. Park, *J. Mater. Chem. C*, 2020, **8**, 6052–6062; (*g*) G. Kreiza, D. Banevičius, J. Jovaišaitė, S. Juršėnas, T. Javorskis, V. Vaitkevičius, E. Orentas and K. Kazlauskas, *J. Mater. Chem. C*, 2020, **8**, 8560–8566.

5 L. S. Cui, H. Nomura, Y. Geng, J. U. Kim, H. Nakanotani and C. Adachi, *Angew. Chem., Int. Ed.*, 2017, **56**, 1571–1575.

6 P. Stachelek, J. S. Ward, P. L. Dos Santos, A. Danos, M. Colella, N. Haase, S. J. Raynes, A. S. Batsanov, M. R. Bryce and A. P. Monkman, *ACS Appl. Mater. Interfaces*, 2019, **11**, 27125–27133.

7 J. Rao, X. Liu, X. Li, L. Yang, L. Zhao, S. Wang, J. Ding and L. Wang, *Angew. Chem., Int. Ed.*, 2020, **59**, 1320–1326.

8 R. Niu, J. Li, D. Liu, R. Dong, W. Wei, H. Tian and C. Shi, *Dyes Pigm.*, 2021, **194**, 109581.

9 J. S. Ward, R. S. Nobuyasu, A. S. Batsanov, P. Data, A. P. Monkman, F. B. Dias and M. R. Bryce, *Chem. Commun.*, 2016, **52**, 2612–2615.

10 S.-J. Woo, Y.-H. Kim and J.-J. Kim, *Chem. Mater.*, 2021, **33**, 5618–5630.

11 (*a*) T. Etienne, *J. Chem. Phys.*, 2015, **142**, 244103; (*b*) S. Grimmea, J. Antony, S. Ehrlich and H. Krieg, *J. Chem. Phys.*, 2010, **132**, 154104.

12 T. Lu and F. Chen, *J. Comput. Chem.*, 2012, **33**, 580–592.